

Wang, Shouzhi; Zhao, Huaping; Lv, Songyang; Jiang, Hehe; Shao, Yongliang; Wu, Yongzhong; Hao, Xiaopeng; Lei, Yong:

Insight into nickel-cobalt oxysulfide nanowires as advanced anode for sodium-ion capacitors

Original published in: Advanced energy materials. - Weinheim : Wiley-VCH. - 11 (2021), 18, art. 2100408, 9 pp.
Original published: 2021-03-21
ISSN: 1614-6840
DOI: [10.1002/aenm.202100408](https://doi.org/10.1002/aenm.202100408)
[Visited: 2021-09-29]



This work is licensed under a [Creative Commons Attribution 4.0 International license](https://creativecommons.org/licenses/by/4.0/). To view a copy of this license, visit <https://creativecommons.org/licenses/by/4.0/>

Insight into Nickel-Cobalt Oxysulfide Nanowires as Advanced Anode for Sodium-Ion Capacitors

Shouzhi Wang, Huaping Zhao, Songyang Lv, Hehe Jiang, Yongliang Shao, Yongzhong Wu, Xiaopeng Hao,* and Yong Lei*

Transition metal oxides have a great potential in sodium-ion capacitors (SICs) due to their pronouncedly higher capacity and low cost. However, their poor conductivity and fragile structure hinder their development. Herein, core-shell-like nickel-cobalt oxysulfide (NCOS) nanowires are synthesized and demonstrated as an advanced SICs anode. The bimetallic oxysulfide with multiple cation valence can promote the sodium ion adsorption and redox reaction, massive defects enable accommodation of the volume change in the sodiation/desodiation process, meanwhile the core-shell-like structure provides abundant channels for fast transfer of sodium ions, thereby synergistically making the NCOS electrode exhibit a high reversible sodium ion storage capacity (1468.5 mAh g⁻¹ at 0.1 A g⁻¹) and an excellent cyclability (90.5% capacity retention after 1000 cycles). The in-situ X-ray diffraction analysis unravels the insertion and conversion mechanism for sodium storage in NCOS, and the enhanced capability of NCOS is further verified by the kinetic analysis and theoretical calculations. Finally, SICs consisting of the NCOS anode and a boron-nitrogen co-doped carbon nanotubes cathode deliver an energy density of 205.7 Wh kg⁻¹, a power density of 22.5 kW kg⁻¹, and an outstanding cycling lifespan. These results indicate an efficient strategy in designing a high-performance anode for sodium storage based on bimetallic dianion compounds.

1. Introduction

Owing to the high abundance and easy availability of sodium reserves, sodium-based electrochemical energy storage technologies, particularly sodium-ion batteries (SIBs), have attracted intensive research interest and achieved significant progress during the past decades.^[1,2] Beyond SIBs, state-of-the-art sodium-ion capacitors (SICs) have now emerged, which the motivation is to combine the advantages of both SIBs (i.e., low-cost and high energy density) and supercapacitors (i.e., high power density and long lifespan) to simultaneously achieve high energy and power density.^[3,4] Although strides have been made in the device design and construction of SICs, the development of high-performance SICs still faces some challenges and drawbacks that have to be overcome, especially with respect to the anode.^[5,6] Since the anode in SICs and its corresponding sodium storage mechanism are exactly the same as that in SIBs, SICs are also suffering from similar chal-


lenging issues arising from the anode as currently faced with SIBs, for example, the large volume expansion of the anode and the sluggish sodium diffusion kinetics in the anode.^[7] Particularly due to the sluggish sodium diffusion kinetics, the diffusion rate of sodium ions in the battery-type anode is much lower than the adsorption/desorption and/or redox reaction rate of anions in the capacitor-type cathode at a high current density.^[8,9] As a result, the non-matched transport rate of cations (i.e., sodium ions) and anions in SICs will lead to the unsatisfied capacity and rate capability of SICs.^[10] Therefore, developing advanced battery-type anode materials plays a pivotal role in achieving SICs with high energy density, high power density, and long-termed cyclability.

Given the high theoretical capacity arising from the multiple electron transfer per metal center, transition metal oxides (TMOs) are of great interest as anodes for SIBs,^[10–12] and some studies also have been carried out on TMOs as anodes for SICs. However, similar problems of serious volume changes, slow redox kinetics, inferior reversibility, and poor conductivity are present.^[13] To this end, binary transition metal oxides (BTMOs, such as MCo₂O₄, M = Ni, Mn, Zn; MMoO₄, M = Ni, Co) and transition metal compounds with multiple anions

Dr. S. Wang, S. Lv, Dr. H. Jiang, Dr. Y. Shao, Prof. Y. Wu, Prof. X. Hao
State Key Lab of Crystal Materials
Shandong University
Jinan 250100, P. R. China
E-mail: xphao@sdu.edu.cn

Dr. S. Wang, Dr. H. Zhao, Prof. Y. Lei
Fachgebiet Angewandte Nanophysik
Institut für Physik & IMN MacroNano
Technische Universität Ilmenau
Unterpoerlitzer Straße 38, 98693 Ilmenau, Germany
E-mail: yong.lei@tu-ilmenau.de

Dr. Y. Shao, Prof. Y. Wu, Prof. X. Hao
Department of Materials Science and Engineering
Qilu University of Technology
Jinan 250353, P. R. China

 The ORCID identification number(s) for the author(s) of this article can be found under <https://doi.org/10.1002/aenm.202100408>.

© 2021 The Authors. Advanced Energy Materials published by Wiley-VCH GmbH. This is an open access article under the terms of the Creative Commons Attribution License, which permits use, distribution and reproduction in any medium, provided the original work is properly cited.

DOI: 10.1002/aenm.202100408

more than the single-oxide ion (e.g., transition metal oxysulfides,^[14] oxynitrides,^[15] and oxycarbides^[16]) have been synthesized and explored as anodes for SIBs as well as potentially for SICs. Compared with TMOs, BTMOs possess significantly improved theoretical capacity and electronic conductivity but their sodium storage capability is still limited by the sluggish sodiation/desodiation reaction kinetics as well as the large volume changes during the charge–discharge processes.^[17] With respect to transition metal compounds with multiple anions beyond single-oxide ion, they also have higher electronic conductivity and higher reversible capacity than those of TMOs, and more importantly, anion substitution enables manipulating the cation band and thus offers the new opportunity to tune the redox potential of anodes.^[18,19] However, due to the difference in anion radius and charge, the intricate short-range atomic ordering will cause the lattice distortion in the bulk phase, resulting in the fragile structure of the disordered crystalline material.^[20] As a result, the transition metal compounds with multiple anions beyond single-oxide ion still face a tough challenge in cyclability due to their fragile structure. Therefore, a comprehensive strategy has to be further developed for rectifying the limitations of TMO-based anode for sodium storage.

Note that creating vacancies in TMOs has been demonstrated as an efficient strategy to optimize the sodium storage capability of TMOs as anode.^[10,12,17,21] On the one hand, the introduction of vacancies in TMOs is a benefit to increasing their electronic conductivity.^[21] On the other hand, the vacancies in the crystal would generate interconnected diffusion channels to facilitate sodium ions' diffusion during the charge–discharge processes.^[22] Pauling pointed out that there will be an open structure in a complex crystal consisting of various ions with different radii when not all of the close-packed positions are occupied by ions.^[20] The missing of ions at some of the close-packed positions means the existence of vacancies in the crystal structure, which should be the reason to form an open structure.^[23] Such an open structure arising from the vacancies might also be advantageous to accommodate the volume change in the sodiation/desodiation process.

Out of the above considerations, herein nickel-cobalt oxysulfide ($\text{NiCo}_2\text{O}_3\text{S}$, depicted as NCOS) nanowires with a core-shell-like structure have been synthesized and demonstrated as high-performance anode for SICs. Structural analysis indicates considerable vacancies on the surface of NCOS nanowires which arise from the deficiency of sulfur atoms at some of the close-packed positions in the crystal structure of NCOS. Electrochemical characterizations demonstrate that the abundant vacancies on the surface of NCOS nanowires enable to efficiently accommodate the volume expansion in the sodiation/desodiation processes, and at the same time promote the rapid sodium ions diffusion in NCOS. Further in-situ X-ray diffraction (XRD) characterizations together with density function theory (DFT) calculations reveal the mechanism of NCOS for improving the sodium storage capability and cycling stability of NCOS as SICs anode. Finally, the assembled SICs with NCOS anode and B, N co-doping carbon nanotubes (BCN) cathode possess high energy density, impressive power density, and excellent cycling lifespan.

2. Results and Discussion

The synthesis process of NCOS is illustrated in **Figure 1a**. Densely ordered Ni–Co precursor nanowires were first prepared on plasma-treated carbon fibers by a hydrothermal method. After the high-temperature sulfidation treatment process, the Ni–Co precursors were further transformed into Ni–Co oxysulfides (i.e., NCOS) through the anion exchange reaction. Compared to Ni–Co precursor nanowires (**Figure S1**, Supporting Information), there are no obvious changes in morphologies of NCOS nanowires and the vertically aligned features have been well preserved (**Figure 1b**), but NCOS nanowires have a unique core-shell-like nanoarchitecture with a tube-like open end (**Figure 1c**). The core-shell-like characteristic of NCOS nanowires was further identified with the high-angle annular dark-field scanning transmission electron microscope (HAADF-STEM), as shown in **Figure 1d**. Clearly, NCOS nanowire has a uniform outer shell with some nanoparticles randomly dispersed in the inner region of the NCOS nanowire. Some voids can also be found among these dispersed nanoparticles, which are formed along with the release of some gases (e.g., CO_2 and H_2O) generated during the sulfidation treatment of Ni–Co precursor at the high temperature.^[5] These voids should be advantageous for accommodating the volume expansion during the sodiation/desodiation processes.^[24] The transmission electron microscopy (TEM) image (**Figure 1e**) again reveals the core-shell-like structure of NCOS. According to the high-resolution TEM (HRTEM) image (**Figure 1f**), the nanoparticles dispersed in the inner region of NCOS nanowire are highly crystalline with the size of about 10 nm, while the outer shell is an obvious layer with a thickness of ≈ 30 nm. The enlarged TEM image of the outer shell shows the clear lattice fringes with an average interlayer spacing of 0.27 nm, corresponding to the (220) plane of hexagonal NiCo_2O_4 (**Figure 1g**),^[25] which also implies that NCOS maintains the hexagonal structure of NiCo_2O_4 after partial substitution of oxygen atoms in NiCo_2O_4 with sulfur atoms. More importantly, many defects are found in the outer shell from the high-resolution TEM image (**Figure 1g**). These defects are caused by the anion exchange, and should be as active sites for improving the electrochemical performance of NCOS.^[14] The energy-dispersive spectroscopy (EDS) analysis (**Figure S2** and **Table S1**, Supporting Information) indicates that the atom ratio of oxygen and sulfur in NCOS is $\approx 3:1$, which is consistent with the inductively coupled plasma optical emission spectroscopy (ICP-OES) test result (**Table S2**, Supporting Information), suggesting the composition of NCOS to be $\text{NiCo}_2\text{O}_3\text{S}$. Furthermore, the relevant EDS mapping images demonstrate the even distributions of the Ni, Co, O, and S elements of the NCOS (**Figure S3**, Supporting Information). For comparison, both NiCo_2O_4 (NCO) and NiCo_2S_4 (NCS) nanowires were also synthesized from the same Ni–Co precursor nanowires by controlling the conditions of thermal annealing and anion exchange processes, and their morphologies and compositions were also carefully characterized with SEM and EDS (**Figures S2** and **S4**, Supporting Information).

XRD analyses were employed to characterize the crystallinity and phase identification of NCOS as well as NCO and NCS. Note that the cobalt target was engaged in order to clearly characterize the crystal structure of the samples. As shown in **Figure 2a**, the peak at 29.76° in all the samples is assigned to the (002) plane

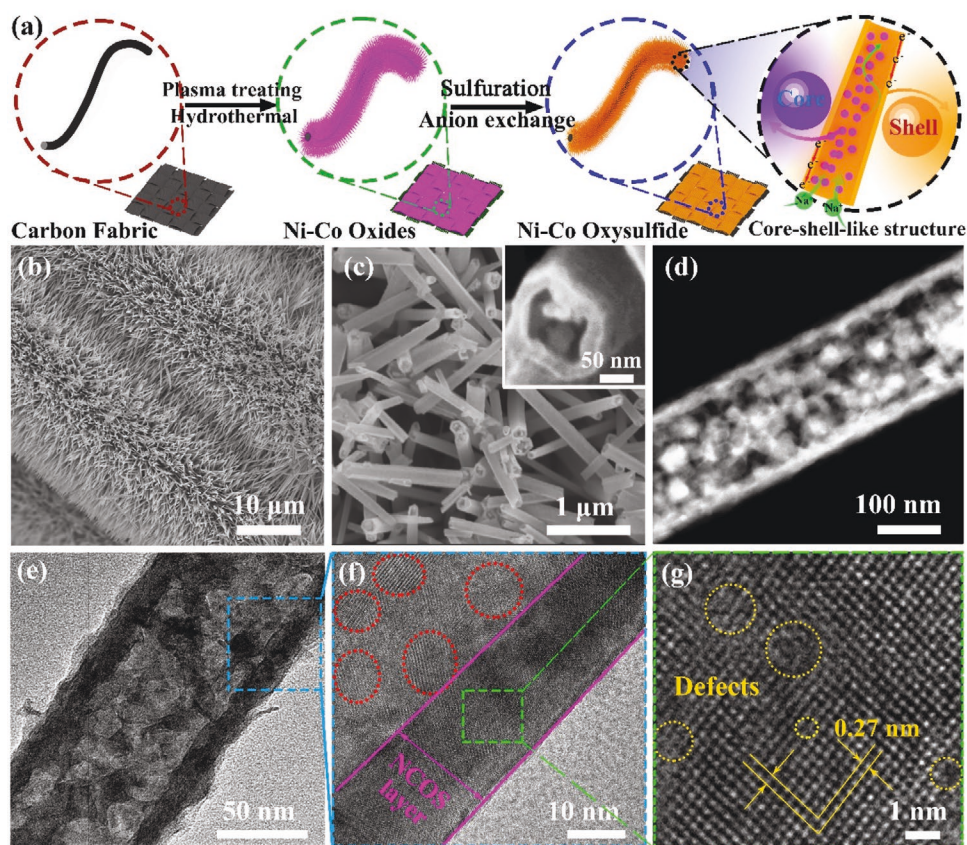


Figure 1. a) Schematic illustration of the fabrication procedure of NCOS with core-shell-like nanoarchitecture; SEM images of NCOS on carbon fabric under low magnification (b) and high magnification (c); the HADDF image of the NCOS (d); TEM images of the NCOS samples in low-magnification (e) and high-resolution (f), and the corresponding high-resolution TEM image (g).

of carbon cloth, while the peak at 44.51° appearing in both NCO and NCOS corresponds to the (311) plane of NiCo_2O_4 (JCPD card No. 20-0781).^[5] The peak at 65.25° in both NCS and NCOS can be assigned to the (440) plane of NiCo_2S_4 (JCPD card No. 20-0782),^[26,27] again suggesting the successful partial substitution of oxygen atoms with sulfur atoms in NCOS. In Raman spectra (Figure 2b), the vibration peak at 517 cm^{-1} is ascribed to the T_{2g} modes in Ni-Co based composites.^[28] The vibration peaks between 100 and 450 cm^{-1} in the Raman spectrum of NCS are attributed to the stretching of S atoms toward the tetrahedral site Ni atom, the bending of S-Ni bonds, and the S-O-Ni bonds.^[29] In addition, Fourier transform infrared spectra (Figure S5, Supporting Information), further confirmed the presence of the Ni/Co-O-S (870 cm^{-1}) in the NCOS.^[30]

The surface oxidation and electronic states of all samples were evaluated by electron paramagnetic resonance (EPR) and X-ray photoelectron spectroscopy (XPS). As shown in Figure 2c, all samples show a special EPR signal with a certain g -value of about 2.002, indicating electrons trapped by surface oxygen vacancies.^[5] The highest electron spin resonance intensity of NCOS indicates the presence of massive oxygen vacancies on the surface, and thus an improved electrochemical performance shall be expected.^[31] Figure S6a, Supporting Information presents the survey spectra of the samples which prove the existence of C, O, Co, and Ni elements in NCO and an additional S

peak in NCOS and NCS. The elemental compositions obtained from XPS results are in accordance to the EDS analysis (Table S2, Supporting Information). As shown in Figure 2d–e, the Ni 2p and Co 2p spectra can be fitted with two and three spin-orbit characteristic peak and relevant shake-up satellites (identified as “Sat.”).^[13] In detail, the peaks at 856.8, 855.6, and 853.5 eV for Ni 2p_{3/2} spectrum correspond to the Ni²⁺, Ni-O-S, and Ni³⁺, respectively.^[29] Similarly, the Co 2p spectrum is fitted with the spin orbit characteristic of Co²⁺, Co-O-S, Co³⁺, and relevant shake-up satellites (Figure 2e). With respect to the O 1s spectra of NCO and NCOS (Figure 2f), the peak at 529.9 eV is ascribed to typical metal-oxygen bonds and the peak at 530.7 eV is generally associated with oxygen defects.^[5] The ratio of the oxygen defects to metal-oxygen bonds in NCOS is obviously higher than that of NCO, suggesting a high content of oxygen defects.^[32] The S 2p spectrum of NCOS and NCS (Figure 2g) is corresponding to the 2p_{1/2} and 2p_{3/2} peak, while the peak at 162.8 and 161.8 eV are attributed to the metal-sulfur bonds.^[33] Note that the metal-sulfur bonds are believed to be favorable for the sodiation/desodiation process.^[19]

The sodium storage performance of NCOS was first evaluated by assembling half-cell SIBs. Figure 3a shows the initial five cyclic voltammetry (CV) curves of NCOS electrode at a scan rate of 0.2 mV s^{-1} in a potential range of 0.01–3.0 V. The nearly overlapped CV curves after the first cycle demonstrate

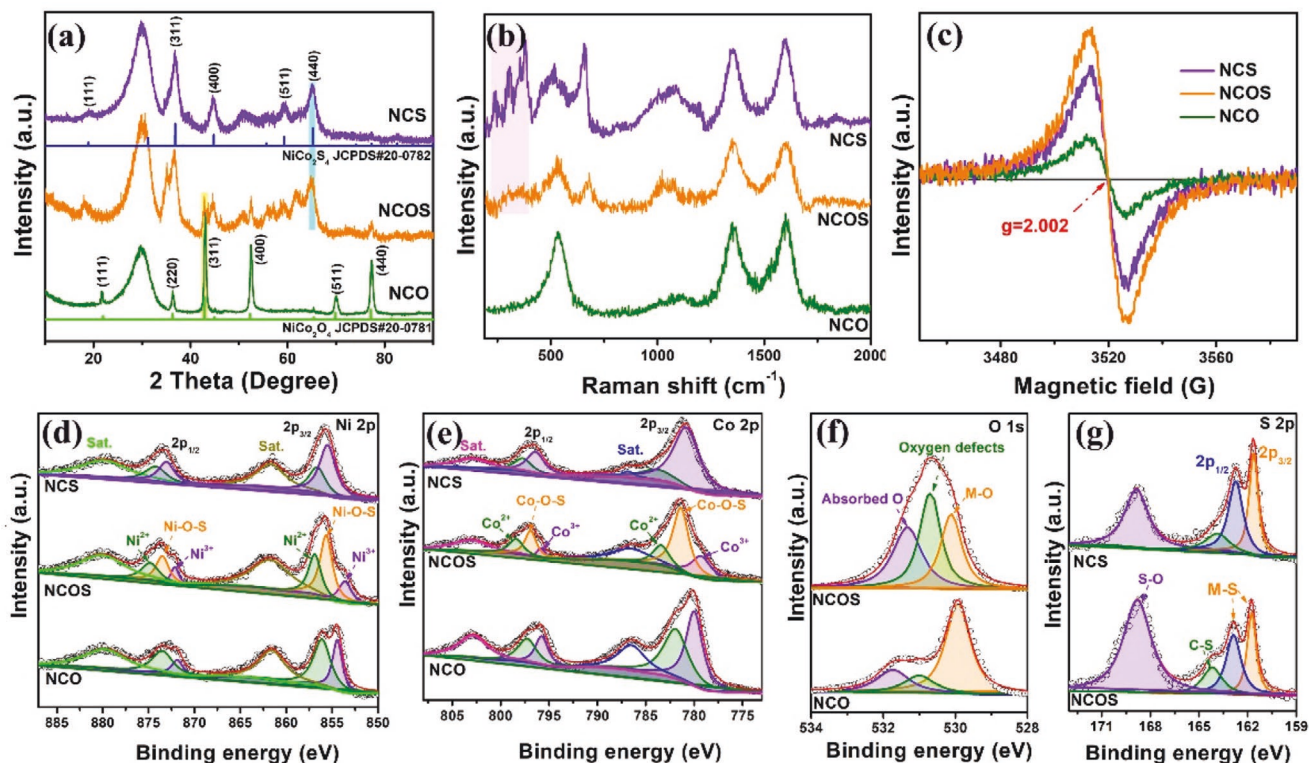


Figure 2. Structure characterizations of the Ni–Co based samples. a) XRD patterns; b) Raman spectra; c) EPR spectra; and the high-resolution XPS spectra of d) Ni 2p, e) Co 2p, f) O 1s, and g) S 2p.

the excellent reversibility for sodiation/desodiation of the NCOS electrode. Broad peaks at 1.18 and 0.76 V are observed for the initial discharge, which can be ascribed to the stepwise sodiation of $\text{NiCo}_2\text{O}_3\text{S}$ to $\text{Na}_x\text{NiCo}_2\text{O}_3\text{S}$ alloys and the formation of a solid-electrolyte interface (SEI) film, respectively,^[24] while the peak at 1.92 V in the anodic scans corresponds to the dealloying and/or conversion reactions. The typical charge–discharge curves of NCOS electrode for the first five cycles at 0.1 A g^{-1} are presented in Figure 3b. The plateau regions in the charge/discharge profiles are consistent with the CV curves. As can be seen in Figure 3b, the initial Columbic efficiency is 73.2%, and this capacity loss can be ascribed to irreversible processes in the first charge–discharge cycle, such as side reactions and SEI film formation.^[34] For comparison, CV curves and charge/discharge profiles of NCO and NCS electrodes indicate the low capacity and rate capability of NCO and NCS electrodes (Figure S7, Supporting Information).

The rate capability of NCOS, NCO, and NCS electrodes were tested by charging–discharging at increasing current densities. As shown in Figure 3c, NCOS delivers the capacities of 1468.5, 1015.0, 531.3, and 320.5 mAh g^{-1} at 0.1, 1.0, 5.0, and 10.0 A g^{-1} , respectively, which are higher than those of NCO and NCS at all current densities, especially at high rates. Note that before the rate performance measurement, a one-cycle CV test was conducted for the as-assembled batteries to ensure these were working well. After cycling at different current densities, the capacity of NCOS recovers 1363 mAh g^{-1} when the current density resets to 0.1 A g^{-1} , which is higher than that of NCO (493 mAh g^{-1}) and NCS (1130 mAh g^{-1}), demonstrating the excellent rate performance of NCOS. Furthermore, the cycling performance are also

compared (Figure 3d). Even after 1000 cycles at 2.0 A g^{-1} , the capacity of NCOS electrode remains 90.5%, while 48.2% for NCO electrode and 32.4% for NCS electrode. In addition, the charge and discharge efficiency of NCOS electrode remains nearly 100% even after 1000 cycles, and there are no significant structural changes of the NCOS electrode (Figure S8, Supporting Information). Note that the cycling performance and specific capacity of NCOS are among the best one of transition metal oxides/sulfide electrodes reported in the literatures (Table S3, Supporting Information). Moreover, the Nyquist plot of the NCOS electrode shows a smaller semicircle in the high frequency and larger slop in the low frequency than that of NCO and NCS (Figure S9, Supporting Information), suggesting the higher conductivity and faster ion diffusion ability of NCOS electrode.^[35]

Generally, the pseudocapacitive storage mechanism can be revealed by the dependence of the current (i) on scan rate (v) obeying the power law $i = av^b$, where a and b are appropriate values.^[15] From the obtained b value, the electrochemical reactions between the diffusion-controlled insertion processes ($b = 0.5$) and surface capacitive ($b = 1$) can be classified. As shown in Figure 3e, the cathodic and anodic b values are 0.86 and 0.88 from the CV curves of NCOS (Figure S10, Supporting Information), respectively, indicating the combined diffusion-controlled insertion process and surface capacitive reaction, and that the surface capacitive reaction is dominant. More specifically, the contributions of surface capacitive and diffusion-controlled insertion reactions can be quantitatively separated.^[36] It can be calculated that the capacitive contribution is about 70.1% of the total capacity of NCOS anode at 0.8 mV s^{-1}

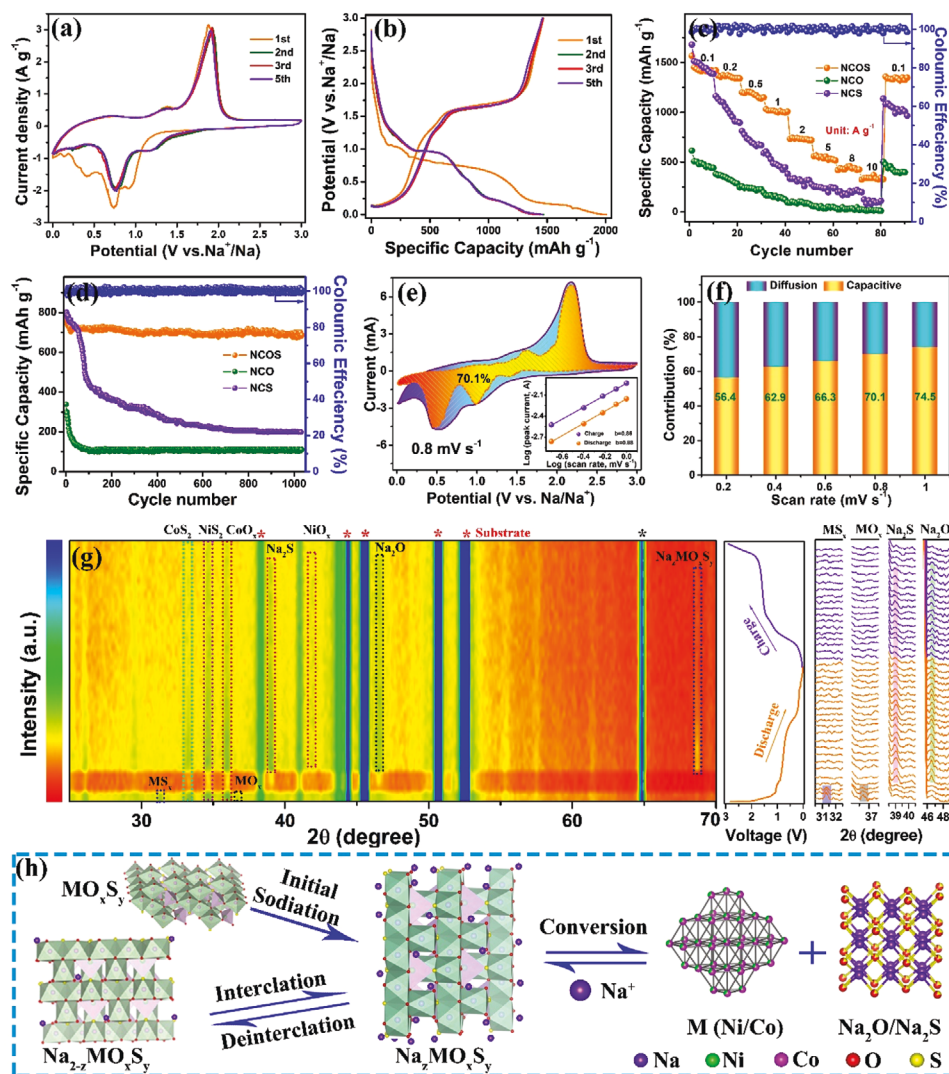
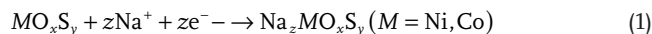


Figure 3. Electrochemical properties of NCOS. a) CV curves of the NCOS electrode at a scan rate of 0.2 mV s^{-1} ; b) GCD profiles of the NCOS at 0.1 A g^{-1} ; c) rate performance at various current densities; d) cycling performance at 2.0 A g^{-1} ; e) separation of capacitive and diffusion current at 0.8 mV s^{-1} , inset shows the measurement of b -value; f) contribution ratios of the capacitive process at different scan rates; and g) in-situ XRD patterns of NCOS electrode during discharge/charge process. h) Schematic illustration of the sodium storage mechanism of the NCOS during the energy storage process.

(Figure 3e), and the ratio of capacitive contribution is enhanced with the scan rate increased (Figure 3f). The high capacitive contribution of NCOS anode could be attributed to the core-shell-like nanostructure with missives active sites that facilitate sodium ion intercalation/deintercalation.^[37]

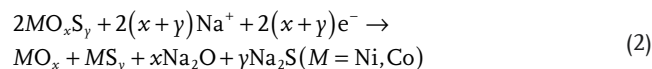
To further make insight into the kinetic behavior of Na ion in NCOS anode, the operando XRD characterizations were performed (Figure 3g). It is obvious that the densities of two peaks of MO_x and MS_y ($M = \text{Ni, Co}$) located at 31.4° and 36.7° decrease during the discharge process in the first cycle, which means the NCOS has participated in the sodiation reaction. Nevertheless, these peaks do not return to its initial position in the charge state, indicating the irreversible reaction. The peak of intermediate product ($\text{Na}_z\text{MO}_x\text{S}_y$) at 67.9° is also detected in the discharge process of first cycle,^[38] which confirms the small lattice spacing expansion and contraction of partial sodiation product $\text{Na}_z\text{MO}_x\text{S}_y$

caused by the insertion and extraction of sodium ions, the relevant intercalation reaction of NCOS is proposed as following:^[12]



Notably, the peaks at 39.2° (Na_2O) and 49.5° (Na_2S) appear and become much stronger in the sodiation and desodiation process, the relevant conversion reaction of the these stages of evolution could be described as the following equation:

First cycle:



Second cycle and beyond:

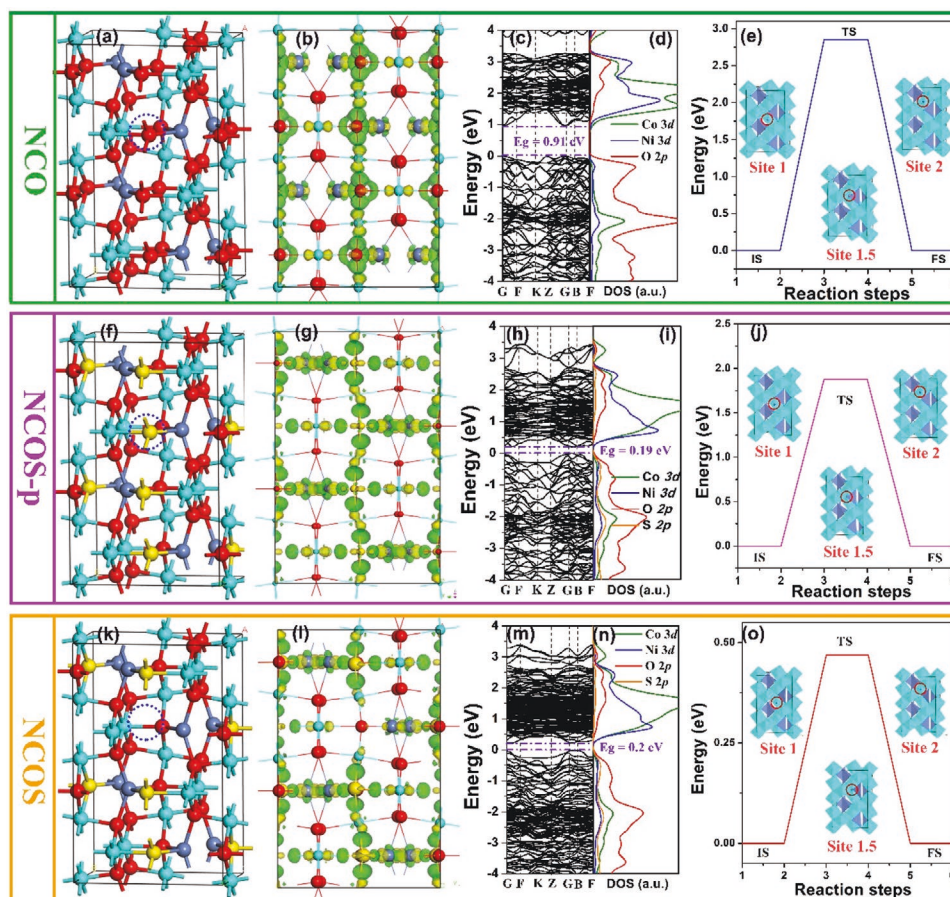
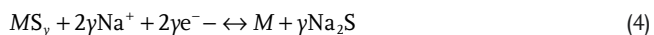
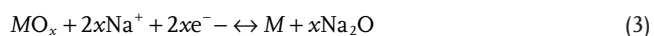


Figure 4. The calculation models of the NCO (a), NCOS-p (f) and NCOS (k), charge-density differences of the NCO (b), NCOS-p (g) and NCOS (l), the red, yellow, light blue, and dark gray spheres for oxygen, sulfide, nickel, and cobalt atoms, respectively; the calculated bandgap structures (c,h,m) and partial density of states (d,i,n) for NCO, NCOS-p, and NCOS; the energy minimum diffusion pathway of a Na⁺ on the e) NCO, j) NCOS-p, and o) NCOS structures; inset shows the calculation models of Na ion inserting into the structures lattices for the initial states (IS, site 1), the transition states (TS, site 1.5), and the final states (FS, site 2), respectively.



Based on the above analysis, Figure 3h illustrates the corresponding reaction schematic of sodium storage mechanism in NCOS, involving the intercalation reaction and the bimetallic conversion reaction which the bimetallic conversion is the dominant one.

DFT calculations were further performed in order to comprehensively understand the effect of mix-anions on the electron properties and the internal Na⁺ storage mechanism of NCOS. According to EPR, XPS, and TEM results, some oxygen vacancies are introduced in NCOS when O atoms are replaced by S atoms with the ratio of O/S = 3/1. Besides NCOS with vacancies, we also design defect-free NCOS (depicted as NCOS-p) for comparison. Ideally, no vacancy will be generated when one oxygen atom of NCO (the encircled area in Figure 4a) is exactly substituted with one sulfur atom (the encircled area in Figure 4f). But in the case of NCOS, oxygen vacancies (the encircled area in Figure 4k) are formed due to the incomplete substitution

of oxygen atoms in NCO by insufficient sulfur atoms. Compared with the crystal structure of NCO (Figure 4a), there is no obvious structural distortion in the crystal structure of both NCOS-p (Figure 4f) and NCOS (Figure 4k), although there is an obvious oxygen vacancy in NCOS (marked in Figure 4k).^[5] As shown in Figures 4b, 4g and 4l, the charge densities of NCO, NCOS-p, and NCOS are obviously different. For NCOS and NCOS-p, the charge around the sulfur atom increases significantly compared with that of NCO, indicating its enhanced electronegativity and then further improved conductivity of NCOS.^[13,39] To investigate the effect of S doping on the electronic structures of NCOS, the partial density of states (PDOSs) was also calculated. It can be seen from Figures 4i and 4n that NCOS-p and NCOS introduce a much wider S 3p impurity state near the Fermi level that mixes with O 2p states, resulting in the lower bandgap of NCOS-p (0.19 eV, Figure 4h) and NCOS (0.20 eV, Figure 4m) than that of NCO (0.91 eV, Figure 4c). In addition, after S atoms have partially substituted O atoms, the state density of NCOS displays a slight delocalization (Figure 4i,n). Due to the higher electronegativity and longer bond length of Ni/Co–S and Ni/Co–O–S bonds than those of Ni/Co–O bonds, the attraction for 3d electrons of

$\text{Co}^{3+}/\text{Co}^{2+}/\text{Co}^+$ or $\text{Ni}^{3+}/\text{Ni}^{2+}/\text{Ni}^+$ in NCOS is weakened, and the energy in the electron transport redox reaction is reduced, thus the reaction kinetics could be greatly improved.^[40] These results again identify that the conductivity of NCOS is further improved after S atoms being introduced.

The outstanding sodium ion storage performance of the NCOS is also related to the localized migration energy barriers of Na^+ ions. Periodic structures of NCO, NCOS, and NCOS-p are shown in Figures 4a, 4f, and 4k. The diffusion path for Na^+ is evaluated by the nudged elastic band method and corresponding migration energy barriers are obtained.^[39] The migration pathway of the three models is from a hollow site 1 to a nearby spaced hollow site 2, as shown in Figures 4e, 4j, and 4o, the diffusion energy barrier of Na^+ in NCO, NCOS-p, and NCOS are 2.46, 1.87, and 0.46 eV, respectively, indicating the highest mobility of Na^+ in NCOS. The detailed calculation process is shown in Table S4 and Experimental Methods, Supporting Information. After Na^+ reaction, the corresponding formation energy (E_f) values of NCO (-2.49 eV), NCOS-p (-2.97 eV), and NCOS (-3.41 eV) indicate that Na^+ on NCOS is the most stable. This result confirms that NCOS possesses much stronger binding with Na^+ , corresponding with the increased specific capacity.^[39]

To further evaluate the potential of NCOS as SIC anode, SICs were assembled by employing NCOS as anode and BCN as cathode (Figure 5a). Note that BCN grown on carbon cloth was designed to enlarge the voltage window of the device.^[41]

NCOS electrode was presodiated to 0.8 V by directly contacting with sodium metal in the electrolyte before assembling the device.^[42,43] Meanwhile, according to the charge balancing theory, $Q^+ \text{ m}^- = Q^- \text{ m}^-$,^[5] the mass loading of the electrodes has undergone a series of adjustments to achieve the best electrochemical performance. The electrochemical properties of BCN electrode was tested in Na^+ half-cell in the potential range of 2.0–4.5 V (versus Na/Na^+) which is characterized in the Figure S11, Supporting Information. Furthermore, the BCN electrode delivers outstanding capacitance and cycling performance, as shown in Figure S11, Supporting Information, which also identifies that the BCN electrode is an excellent potential SIC cathode. As predicted, the operation window for SICs reached 0–4.5 V (Figure 5b). Figure 5c displays the GCD profiles of the NCOS//BCN device. The shapes of charging and discharging curves are almost symmetric under varied current densities, revealing the high reversibility. A similar phenomenon can also be observed from the capacitances versus scan rate and current density; the capacitance can also be retained. As shown in Figure 5d, the capacitance of SIC is 73.2 F g^{-1} at 50 mA g^{-1} , and the capacitance remains 37.5 F g^{-1} when increasing the current density up to 10 A g^{-1} . More importantly, the capacity of the NCOS//BCN SIC retains of 90.0% after 10 000 cycles at 10 A g^{-1} (Figure 5e), which implies the excellent cycling stability.

The Ragone plot (Figure 5f) shows that the assembled NCOS//BCN SIC delivers a high energy density of

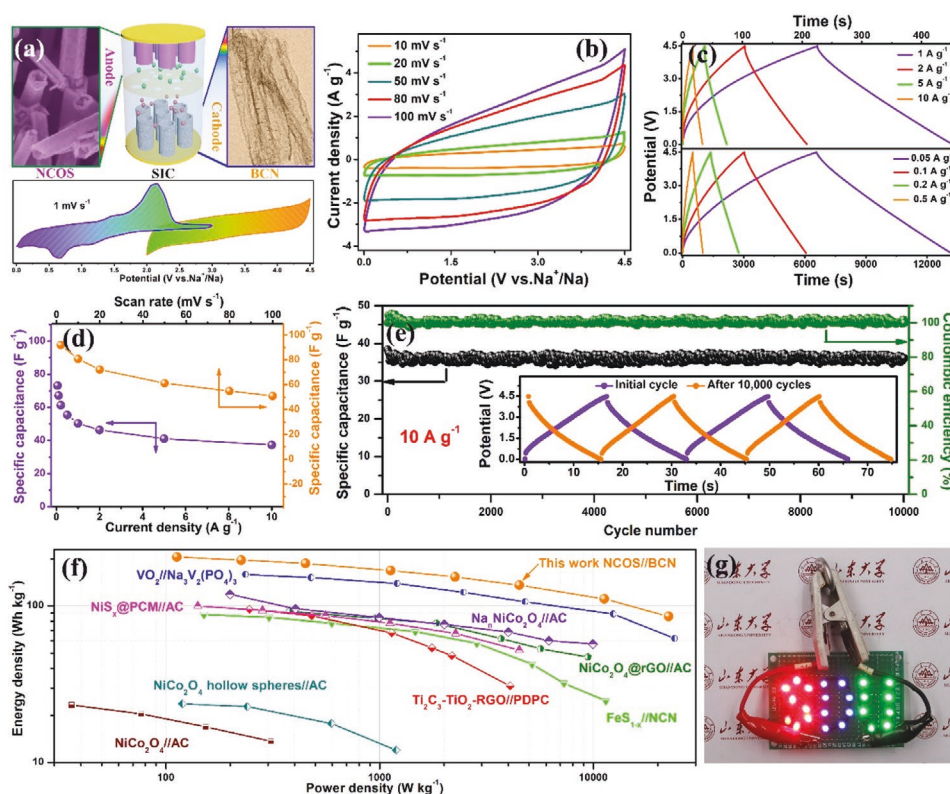


Figure 5. Electrochemical performance of NCOS//BCN SICs. a) Schematic of the assembled SIC device (inset shows diagram of the operation potential range for configuration); b) CV curves at various current densities; c) GCD curves at increasing current densities; d) capacitances as a function of scan rate and current density; e) cycling performance, insert shows GCD curves before and after cycle; f) Ragone plots in comparison with other SICs reported in literature; and g) shows the image of commercial LEDs powered by the fabricated SICs.

205.7 Wh kg⁻¹ at a power density of 125 W kg⁻¹ based on the total mass of both electrodes. Even at the power density up to 22 500 W kg⁻¹, it still delivers a high energy density of 85.7 Wh kg⁻¹. The energy and power densities of NCOS//BCN SIC are higher than those of many other state-of-the-art SICs such as VO₂//Na₃V₂(PO₄)₃,^[44] NiS_x@PCM//AC,^[45] Na_nNiCo₂O₄//AC,^[46] Ti₂C₃-TiO₂-RGO//POPC,^[47] NiCo₂O₄@rGO//AC,^[17] NiCo₂O₄ hollow sphere//AC,^[48] NiCo₂O₄//AC,^[49] and Fe_{1-x}S//NCN devices^[50] (Figure 5f and Table S5, Supporting Information). In addition, the SICs device also displays a high areal energy density of 58.11 μWh cm⁻², as shown in Figure S12, Supporting Information. Furthermore, a fully charged NCOS//BCN SIC device could power 24 commercial light-emitting diode (LED) lights (Figure 5g) in a proof-of-concept experiment. Overall, these merits of the NCOS//BCN SIC device with high-voltage output, excellent energy and power density, as well as cycling life, show great potential for future electrochemical energy storage applications.

3. Conclusion

In summary, core-shell-like NCOS nanowires were synthesized as the superior anode for SICs. The massive vacancies, multivalent metal cations, and ample voids in NCOS endow to achieve an excellent sodium storage performance with an ultrahigh reversible specific capacity of 1453 mA h g⁻¹ at 100 mA g⁻¹. The intercalation and conversion reaction mechanism of sodium storage in NCOS was identified via in-situ XRD analysis during the reversible reaction process. The DFT calculation results proved that the weakened bond energy of Ni/Co—O—S bonds in the NCOS can decrease the electron transport energy during the energy storage, then further improve the reaction kinetics. Finally, the NCOS-based SICs were assembled and exhibited a high energy storage capability, that is, an energy density of 205.7 Wh kg⁻¹, a power density of 22.5 kW kg⁻¹, and an excellent cycle stability. This work gives insights into the design of metal oxide-based electrodes with a satisfying energy and power density for next-generation SICs.

4. Experimental Section

Preparation of Ni—Co-Based Composites: Nickel chloride hexahydrate (2.5 mm), cobalt hexahydrate (5 mm), and urea (9 mm) were dissolved in 32 mL DI water, then the air plasma-treated carbon cloth was put into the above solution for 20 min. Thereafter, the solution together with the carbon cloth were transferred to a Teflon-lined stainless autoclave (40 mL) and heated at 130 °C for 6 h. The as-prepared precursors grown on carbon cloth carbon were washed several times with DI water and ethanol, and dried overnight at 80 °C. Finally, the prepared sample was further placed in a 50 mL Teflon-lined stainless-steel autoclave with a solution containing 40 mL of 0.1 M sodium sulfide, and the autoclave was sealed and maintained at 120 °C for 2 h, to prepare a NiCo₂O₃S composite (NCOS). As a comparative sample, the Ni—Co precursor was annealed at 350 °C for 2 h in Ar atmosphere to obtain a NiCo₂O₄ sample (NCO), and the Ni—Co precursor was placed in a same sodium sulfide solution, heated at 120 °C for 6 h to obtain a binary transition metal sulfide sample (NCS).

Fabrication of Sodium-Ion Capacitors: The presodiated NCOS anode and BCN cathode were directly used as self-supporting electrode. The device was assembled into coin-type test cell (CR2032) in an argon-filled glove box. The electrolyte was 1 M NaClO₄ in ethyl carbonate/dimethyl

carbonate (DMC) + fluoroethylene carbonate (FEC) (EC:DMC = 1:1 by volume ratio, 5 wt% FEC) and glass microfiber filter as the separator. In the assembled SIC device with optimal performance, the mass loading of the negative and positive electrodes were ≈1.0 and 3.0 mg cm⁻², respectively. The thickness of the electrode (including carbon cloth) was about 3.1 μm, and the total area of the device was 3.14 cm⁻².

Supporting Information

Supporting Information is available from the Wiley Online Library or from the author.

Acknowledgements

S.W. and H.Z. contributed equally to this work. This work was supported by NSFC (51872162 and 11890700), Natural Science Foundation of Shandong Province (ZR2020QE064), Postdoctoral Innovation Foundation of Shandong Province (202001001), China Postdoctoral Science Foundation (2019TQ0172 and 2019M662349), German Research Foundation (DFG: LE 2249/5-1), and Sino-German Center for Research Promotion (GZ1579).

Open access funding enabled and organized by Projekt DEAL.

Conflict of Interest

The authors declare no conflict of interest.

Data Availability Statement

The data that supports the findings of this study are available in the supplementary material of this article.

Keywords

bimetallic oxysulfides, density function theory calculations, in-situ XRD, integrated anodes, sodium-ion capacitors

Received: February 3, 2021

Revised: March 6, 2021

Published online: March 21, 2021

- [1] H. Zhao, Y. Lei, *Adv. Energy Mater.* **2020**, *10*, 2001460.
- [2] Y. Zhang, Q. Ma, S. Wang, X. Liu, L. Li, *ACS Nano* **2018**, *12*, 4824.
- [3] H. Zhao, L. Liu, R. Vellacheri, Y. Lei, *Adv. Sci.* **2017**, *4*, 1700188.
- [4] Z. Lei, L. Liu, H. Zhao, F. Liang, S. Chang, L. Li, Y. Zhang, Z. Lin, J. Kröger, Y. Lei, *Nat. Commun.* **2020**, *11*, 299.
- [5] S. Wang, L. Li, W. He, Y. Shao, Y. Li, Y. Wu, X. Hao, *Adv. Funct. Mater.* **2020**, *30*, 2000350.
- [6] J. Ding, H. Wang, Z. Li, K. Cui, D. Karpuzov, X. Tan, A. Kohandehghan, D. Mitlin, *Energy Environ. Sci.* **2015**, *8*, 941.
- [7] L. Shen, Y. Wang, F. Wu, I. Moudrakovski, P. Aken, J. Maier, Y. Yu, *Angew. Chem., Int. Ed.* **2019**, *58*, 7238.
- [8] X. Deng, K. Zou, P. Cai, B. Wang, H. Hou, G. Zou, X. Ji, *Small Methods* **2020**, *4*, 2000401.
- [9] Z. Xu, M. Wu, Z. Chen, C. Chen, J. Yang, T. Feng, E. Paek, D. Mitlin, *Adv. Sci.* **2019**, *6*, 1802272.
- [10] S. Fang, D. Bresser, S. Passerini, *Adv. Energy Mater.* **2020**, *30*, 1902485.

- [11] C. Yuan, H. Wu, Y. Xie, X. Lou, *Angew. Chem., Int. Ed.* **2014**, *53*, 1488.
- [12] J. Lee, G. Singh, W. Cha, S. Kim, J. Yi, S. Hwang, A. Vinu, *ACS Energy Lett.* **2020**, *5*, 1939.
- [13] S. Wang, L. Li, Y. Shao, L. Zhang, Y. Li, Y. Wu, X. Hao, *Adv. Mater.* **2019**, *31*, 1806088.
- [14] K. Chiu, L. Lin, *J. Mater. Chem. A* **2019**, *7*, 4626.
- [15] S. Wang, H. Li, W. He, H. Jiang, Y. Shao, Y. Wu, X. Hao, *J. Energy Chem.* **2021**, *56*, 56.
- [16] J. Cuan, Y. Zhou, J. Zhang, T. Zhou, G. Liang, S. Li, X. Yu, W. Pang, Z. Guo, *ACS Nano* **2019**, *13*, 11665.
- [17] D. Yang, Q. Zhao, L. Huang, B. Xu, N. Kumar, X. Zhao, *J. Mater. Chem. A* **2018**, *6*, 14146.
- [18] H. Kageyama, K. Hayashi, K. Maeda, J. Attfield, Z. Hiroi, J. Rondinelli, K. Poeppelmeier, *Nat. Commun.* **2018**, *9*, 772.
- [19] Q. Guo, Y. Ma, T. Chen, Q. Xia, M. Yang, H. Xia, Y. Yu, *ACS Nano* **2017**, *11*, 12658.
- [20] L. Pauling, *J. Am. Chem. Soc.* **1929**, *51*, 1010.
- [21] Y. Xu, M. Zhou, X. Wang, C. Wang, L. Liang, F. Grote, M. Wu, Y. Mi, Y. Lei, *Angew. Chem., Int. Ed.* **2015**, *54*, 8768.
- [22] S. Wang, L. Zhang, C. Sun, Y. Shao, Y. Wu, X. Hao, *Adv. Mater.* **2016**, *28*, 3768.
- [23] Y. Ye, F. Wu, Y. Liu, T. Zhao, J. Qian, Y. Xing, W. Li, J. Huang, L. Li, Q. Huang, X. Bai, R. Chen, *Adv. Mater.* **2017**, *29*, 1700598.
- [24] K. Yang, J. Tang, Y. Liu, M. Kong, B. Zhou, Y. Shang, W.-H. Zhang, *ACS Nano* **2020**, *14*, 5728.
- [25] A. Shanmugavani, R. K. Selvan, *Electrochim. Acta* **2016**, *189*, 283.
- [26] J. Xiao, L. Wan, S. Yang, F. Xiao, S. Wang, *Nano Lett.* **2014**, *14*, 831.
- [27] S. Wang, J. Zhu, Y. Shao, W. Li, Y. Wu, X. Hao, *Chem. - Eur. J.* **2017**, *23*, 3438.
- [28] S. Wang, Y. Shao, W. Liu, Y. Wu, X. Hao, *J. Mater. Chem. A* **2018**, *6*, 13215.
- [29] X. Wang, S. Zhao, L. Dong, Q. Lu, J. Zhu, C. Nan, *Energy Storage Mater.* **2017**, *6*, 180.
- [30] S. H. Park, Y.-K. Sun, K. S. Park, K. S. Nahm, Y. S. Lee, M. Yoshio, *Electrochim. Acta* **2002**, *47*, 1721.
- [31] S. Liu, Y. Yin, D. Ni, K. S. Hui, M. Ma, S. Park, K. N. Hui, C.-Y. Ouyang, S. C. Jun, *Energy Storage Mater.* **2019**, *22*, 384.
- [32] J. Yu, B.-Q. Li, C.-X. Zhao, Q. Zhang, *Energy Environ. Sci.* **2020**, *13*, 3253.
- [33] L. Zhou, K. Zhang, J. Sheng, Q. An, Z. Tao, Y.-M. Kang, J. Chen, L. Mai, *Nano Energy* **2017**, *35*, 281.
- [34] X. Li, M. Sun, J. Ni, L. Li, *Adv. Energy Mater.* **2019**, *9*, 1901096.
- [35] S. Wang, L. Gai, J. Zhou, H. Jiang, Y. Sun, H. Zhang, *J. Phys. Chem. C* **2015**, *119*, 3881.
- [36] V. Augustyn, J. Come, M. Lowe, J. Kim, P. Taberna, S. Tolbert, H. Abruña, P. Simon, B. Dunn, *Nat. Mater.* **2013**, *12*, 518.
- [37] E. Lim, C. Jo, M. Kim, M. Kim, J. Chun, H. Kim, J. Park, K. Roh, K. Kang, S. Yoon, J. Lee, *Adv. Funct. Mater.* **2016**, *26*, 3711.
- [38] W. Chen, X. Zhang, L. Mi, C. Liu, J. Zhang, S. Cui, X. Feng, Y. Cao, C. Shen, *Adv. Mater.* **2019**, *31*, 1806664.
- [39] Y. Zou, Y. Gu, B. Hui, X. Yang, H. Liu, S. Chen, R. Cai, J. Sun, X. Zhang, D. Yang, *Adv. Energy Mater.* **2020**, *10*, 1904147.
- [40] T. Zhai, L. Wan, S. Sun, Q. Chen, J. Sun, Q. Xia, *Adv. Mater.* **2017**, *29*, 1604167.
- [41] H. Jiang, D. Shi, X. Sun, S. Wang, Y. Li, B. Zhang, B. Zhang, Y. Shao, Y. Wu, X. Hao, *ACS Appl. Mater. Interfaces* **2020**, *12*, 47425.
- [42] K. Kim, G. Ali, K. Chung, C. Yoon, H. Yashiro, Y. Sun, J. Lu, K. Amine, S. Myung, *Nano Lett.* **2014**, *14*, 416.
- [43] Z. Fan, C. Wei, L. Yu, Z. Xia, J. Cai, Z. Tian, G. Zou, S. X. Dou, J. Sun, *ACS Nano* **2020**, *14*, 867.
- [44] D. Xu, D. Chao, H. Wang, Y. Gong, R. Wang, B. He, X. Hu, H. Fan, *Adv. Energy Mater.* **2018**, *8*, 1702769.
- [45] S. Li, W. He, B. Liu, J. Cui, X. Wang, D. Peng, B. Liu, B. Qu, *Energy Storage Mater.* **2020**, *25*, 636.
- [46] D. Yang, X. Sun, K. Lim, R. Gaddam, N. Kumar, K. Kang, X. Zhao, *J. Power Sources* **2017**, *362*, 358.
- [47] R. Wang, S. Wang, Y. Zhang, D. Jin, X. Tao, L. Zhang, *J. Mater. Chem. A* **2018**, *6*, 1017.
- [48] Y. Liu, Z. Wang, Y. Zhong, M. Tade, W. Zhou, Z. Shao, *Adv. Funct. Mater.* **2017**, *27*, 1701229.
- [49] R. Ding, L. Qi, H. Wang, *Electrochim. Acta* **2013**, *114*, 726.
- [50] S. Li, J. Chen, X. Gong, J. Wang, P. Lee, *Small* **2018**, *14*, 1804035.